

# Classification of astrophysical events from gravitational wave signature

Shashwat Singh<sup>1,\*</sup>, Amitesh Singh<sup>1</sup>, Ankul Prajapati<sup>1</sup> and Kamlesh N Pathak<sup>1</sup>  
<sup>1</sup>*Bose.X, Sardar Vallabhbhai National Institute of Technology, Surat, India- 395007*  
*\*u17me090@med.svnit.ac.in*

## ABSTRACT

In recent years, improvements in Deep Learning techniques towards Gravitational Wave astronomy have led to a significant rise in various classification algorithms' development. A few of these algorithms have been successfully employed to search Gravitational Waves from binary Blackhole merger events. However, these algorithms still lack success with significant time duration and further prediction of the merger event's parameters. In this work, we intended to advance the boundaries of Deep-Learning techniques, using the Convolutional Neural Networks, to go beyond binary classification and predicting complicated features that possess physical significance. This method is not a replacement for the already established and thoroughly examined methods like matched filtering for the detection of gravitational waves but is an alternative method wherein human interference is minimal. The DL model we present has been trained on 12s of data segment, aimed to predict the 27 features of any LIGO time-series data. During training, the maximum accuracy attained was 90.93%, with a validation accuracy of 89.97%.

**Keywords:** *Gravitational Waves, Deep Learning, CNN, Multi-label classification*

## 1. INTRODUCTION

Gravitational Waves (GWs) are the disturbances in spacetime, generated by the highly energetic astrophysical events, high enough to disturb the spacetime itself. The highly energetic astrophysical events are the source for this radiant energy that propagates in the form ripples traversing the universe, away from the source. The quadrupole formula of the GWs implies that they can be produced only with extremely high mass ranges and speeds closer to the relativistic limit. Weinberg (July 1972.). Moreover, they have weakly interacting nature with all known matter in Standard Model, further making them difficult to detect; thus, slight changes in spacetime strain goes undetected. Only astrophysical events with high energy sources are suitable candidates from where GW can be produced, as outlined in the Bernard F. Schutz (2009) review. The GWs once merely predictions were strongly confirmed by the LIGO-Virgo observatory on September 15, 2015, when LIGO heard first chirp: GW150914, Abbott et al. (2016a)- which was a Blackhole binary collision event. Further, within two years, with improvement in the interferometer's sensitivity, nine other binary black hole merger events were detected. The O1 running from Sep 12<sup>th</sup> 2015 to Jan 19<sup>th</sup> 2016 with the first run of Advanced LIGO gave observations GW151012, GW151226, and O2 data that ran from November 30<sup>th</sup> 2016, to August 25<sup>th</sup> 2017, with the second run of Advanced LIGO and first run of advanced Virgo observatories resulted in the following merger events: GW170104, GW170608, GW170729, GW170809, GW170814, GW170818 and GW170823, and single detection of GWs from the binary of neutron star, GW170817. The third observing run (O3) running since April 1, 2019, it is divided (so far) into O3a, from 1<sup>st</sup> April to 30<sup>th</sup> September 2019, and O3b, from 1<sup>st</sup> November 2019 to the present (as on December 2019). It has made 39 detections (so far) and is expected to increase predictions several folds with continuous advancements in detectors.

The Advanced LIGO (aLIGO) and the Advanced Virgo (aVIRGO) are highly sophisticated, highly enhanced Michelson Interferometers with arms extending to 4 kilometers for LIGO and 3 kilometers for VIRGO interferometers, each arm perpendicular to each other. The detectors used measures the spacetime strain induced by a transient change in the continuous GW signal, marking the occurrence of any highly energetic astrophysical event. The event causes the arms lengths to vary corresponding to the wavelength signal, disrupting the coherent interference pattern established by the lasers. Though ideally the coherence pattern should always be maintained at all times until any GW passes through the arm length, but in spite of brilliant efforts made to keep the apparatus completely quiet and undisturbed from external sources the noise usually leaks in the setup resulting in disrupted signal in the channels. The transient change in spacetime curvature is measured in terms of changes in the spacetime-strain value, a dimensionless number:  $\Delta l/l$ , where  $\Delta l$  is the slight change in the arm length due to. is the small change in the arm length due to the passing of GWs? The interferometer produces this strain data as a continuous set of strain values in time, sampled at 16384 Hz for LIGO data, and 20 kHz for Virgo data. For the Advanced LIGO detectors, the calibration is valid above 10 Hz and below 5 kHz. The strain data is publicly available at <https://www.gw-openscience.org/data/> as O1 and O2 data. Further details of the Interferometer design, and how the data is generated can be found in the works of Abramovici et al. (1992).

As mentioned above, data generated by the interferometer is highly sensitive and is prone to unavoidable and unpredictable noise disturbances. Apart from GWs from binaries, the interferometer may also detect signals from other transient sources, such as core-collapse supernovae (CCSNe) [Abbott et al. \(2016b\)](#), gravitational wave orphan memory, cosmic strings [[Damour & Vilenkin \(2000\)](#)], or an unknown astrophysical source. Thereby while matched filtering, a sequence of steps is carried out, such as signal processing, preparing template bank, calculating SNR,  $\chi^2$ -test, and other tests before validating signal. These noise signals superimpose the real signal seldom following a specific pattern and repeating themselves during the run. Most random Non-Gaussian noise can be removed by various signal processing techniques such as bandpass filters and notching, but some noises are insidious and considerably affect the signal either by mimicking or masking a part or whole the real signal resulting into a false alarm (detection). Those noise signals that are repeating, have a significant characteristic, are transient and non-Gaussian in nature known colloquially as glitches. Thus, the data encompasses detailed information of the astrophysical event producing GW and the surrounding physical conditions such as the intensity of seismic vibrations, humidity, temperature, and several other prevailing factors that affect the run. A comprehensive classification and characterization of these noises and their features have been discussed further in [Sec-2.6](#).

In this work, we aim to present a Deep Convolutional Neural Network model that, when fed with the time-series signal of the LIGO data or any time-series spacetime strain data, gives output primarily extracting the GW signal if present, and thereon predicting the features of the signal. Classes that have been used for the model can be classified into trigger events, which include Blackhole binaries (BHB), Neutron stars binaries (NSB), Neutron star Blackhole (NSBH), Gravitational-wave Echoes, Core-collapse supernovae (CCSNe) and Non-Gaussian random noise as well as Glitches. The details of these classes have been discussed in [Sec-2](#). The model we present is efficient in extracting information even from the datasets having Glitches and further predict the presence of GW signal. The central idea exercised is that a signal decomposed into various components, is governed by the Fourier Transform: represented as the sum of sines and cosines. The decomposition of the signal into components had to be done so that each component retains its physical significance. Employing the DL technique, we aimed to extract the wave components which are features in terms of DL techniques. The time-series signal was constructed from the spectrograms using a technique of image to signal some of the dominant glitches as observed in the data quality of the aLIGO for both first and second run. (details in [Sec-4.1.5](#)).

The structure of this paper is as follows: In [Sec-2](#) a brief description regarding the properties of LIGO Data is discussed giving necessary insights to the basic components that form part of the trigger events dataset; noise and a discussion of the glitches, their probable source, features, and the time-series signal generated. [Sec-3](#) focuses on previous works that have been done in this domain going beyond multiclass classification, thereby attempting to fill the gaps towards the development of the GW astronomy. In [Sec-4](#), we discuss the model features and justification for the same; methodology of Data Preparation, Model selection, Model preparation, and thereon justification for the same and finally testing and validation. Finally, we conclude with the discussion of the results in [Sec-5](#).

## 2. DATASET COMPONENTS

LIGO being highly sensitive, even slight variations in the desired operating conditions leads to a *hitch-hike* in the output signal. In this section, we have discussed the aforementioned classes that we have used for our model, assuming them to be the possible candidates detected with the detectors with current sensitivity or those proposed shortly: LIGO-India, KAGRA, LISA. The trigger signals: Blackhole binaries (BHB), Neutron stars binaries (NSB), Neutron star Blackhole (NSBH), Gravitational-wave Echoes, Core-collapse supernovae (CCSNe) and Non-Gaussian random noise, as well as Glitches, have discussed below. Gravitational-wave Echoes, Core-collapse supernovae have been discussed in detail, considering the need to explain the phenomenon due to many proposed models and absence or very few predictions by the detectors from where the simulated data and the physical model can be verified. Below is a discussion on each of the above classes, each subsection describing the fundamental data generation scheme and further developments reflected in the current data generation scheme, the constraint, and the justification for the same.

### 2.1. Black hole binaries

Blackhole binaries can be studied under three-stages of signal generation: inspiral, merger, ringdown. The inspiral part is generated by using Post-Newtonian (PN) approximation solving for the PN parameter  $x = \frac{v^2}{c^2}$  from [Eq-1](#) and the merger part is solved using the semi-analytical method of the original nonlinear equations of General Relativity. The 6-PN term approximant has been used in [Huerta et al. \(2017a\)](#) is the highest order for quasi-circular (QC) orbits. The Taylor T4 approximant for QC-orbits given using [Eq-2](#) and then integrating it using the expansion coefficients given in [Buskirk & Hamilton \(2019\)](#), gives the evolution of  $x$ .

$$\frac{dx}{dt} = \frac{dx^{0PN}}{dt} x^5 + \frac{dx^{1PN}}{dt} x^6 + \frac{dx^{2PN}}{dt} x^7 + \frac{dx^{3PN}}{dt} x^8 + \frac{dx^{HT}}{dt} \quad (1)$$

$$M \frac{dx}{dt} |^{6PN} = \frac{64}{5} \eta x^5 \left( 1 + \sum_{k=12}^{12} a_k x^{\frac{k}{2}} \right) \quad (2)$$

of polarizations namely  $h_{\times}$  and  $h_{+}$ , can be constructed, represented as a function of  $t$ : representing time,  $\theta$  and  $\phi$ , the polar and azimuthal angles for the direction of propagation of GW and  $\lambda$ : set of parameters characterizing the waveform. The two polarized quantities are dimensionless. In fundamental frame assuming the detector's orientation to be normal to the orbital plane, the two polarizations leading to the orbit's inclination angle  $\theta$  to be zero,  $h_{\times}$  and  $h_{+}$  can be evaluated from:

$$h_{+} = -2M\eta \left[ (r^{\dot{2}} + r^2 \dot{\phi}^2 + \frac{M}{r}) \cos 2\Phi + 2r\dot{r}\dot{\phi} \sin 2\Phi \right] \quad (3)$$

$$h_{\times} = -2M\eta \left[ (r^{\dot{2}} + r^2 \dot{\phi}^2 + \frac{M}{r}) \sin 2\Phi + 2r\dot{r}\dot{\phi} \cos 2\Phi \right] \quad (4)$$

$$h(t, \theta, \varphi; \lambda) = h_{+}(t, \theta, \varphi; \lambda) + ih_{\times}(t, \theta, \varphi; \lambda) \quad (5)$$

The modeling of the merger phase requires solving the nonlinear system of General Relativity. So far, analytical methods have been employed due to the huge computational cost and complexity. One of the analytical method *Implicit Rotating Source Method* (IRS) as in [Huerta et al. \(2017b\)](#), the merger can be calculated using Eq-6, and thereon using the equation for amplitude from [Huerta et al. \(2017b\)](#) we can calculate the orbital velocity  $\omega(t) = \omega_{QNM}(1 - \hat{f})$ , where  $\omega_{QNM}$  is the least damped frequency of the Quasi-Normal modes (QNM) radiated by the coalesced black hole, after settling as sphere or ellipsoid in case of extreme spin values. Thus on further integrating the orbital velocity which is the function of time due to the reasons mentioned in inspiral part, we can calculate the phase  $\Phi_{gIRS}$  from  $\Phi_{gIRS}(t) = \int \omega(t) dt$  and thereon using Eq-6 we can calculate  $h^{merger}$ .

$$h^{merger}(t) = A(t) e^{-i\Phi_{gIRS}(t)} \quad (6)$$

Due to fast development in Numerical Relativity (NR), NR-PN hybrid waveform template-banks have been constructed. These surrogate waveforms require a reduced parameter space to generate the waveform [[Baker et al. \(2008\)](#), [Blackman \(2017\)](#)]. NR simulations provide the most precise values for BBH-GW waveforms but are excessively expensive for specific tasks, specifically parameter estimation. Surrogate models of NR waveforms have proved to be fast and accurate. NR surrogate models make no underlying presumptions about the waveform structure and undeviatingly interpolate the NR data across the parameter space. NR being now sufficiently mature since its development, plenty of codes are available ([Lousto & Zlochower 2011a](#)) that are capable of accurately and precisely simulating all the phases of a BHB-system: inspiral, merger and ringdown, thereby the extending results towards extreme spins and high mass ratios [([Lousto & Zlochower 2011b](#)), ([Szilágyi 2014](#))]. In spite of the NR-waveforms being quite accurate, the drawback lies with the computational cost and the calculation time it bears. Thereby surrogate models have been employed to generate the template bank. The NR simulations using Spectral Einstein Code (SpEC) [Varma \(2019\)](#) have been employed as a novel technique to model waveforms. The number of NR simulations required to build a surrogate model largely depends on parameter space size, and becoming more computationally expensive as the mass ratio and spin magnitudes grow. The PyCBC (<https://www.gw-openscience.org/data/>) pipeline enables the use of LALSuite simulations that contain template waveforms for BHB, NSB, and NSBH. In Sec-4.1 we have summarized the PyCBC pipeline and highlighted the sample data generated for the model using the same pipeline.

## 2.2. Neutron star binaries

In this section, we shall discuss the proposed physical mechanisms that occur within the neutron star explaining GW's emission. Spinning neutron stars possessing asymmetric deformations emit GWs. Elastic strains in the crust [[Ushomirsky et al. \(2000\)](#)], or strong magnetic fields in the core [[Zimmermann & Szedenits Jr \(1979\)](#)] is capable enough to create such deformations. Non-axisymmetric deformities on the neutron star can be supported either by elastic stresses in the crust or by magnetic fields represented in terms of the equatorial ellipticity:

$$\epsilon = \frac{I_{xx} - I_{yy}}{I_{zz}}$$

where  $I_{jj}$  are the three principal moments of inertia. A triaxial body rotating about one of its principal moments of inertia will emit radiation at frequency  $f_{gw} = 2\nu$ , where  $\nu$  is the star's spin frequency. More precisely, a freely precessing, axisymmetric body, with principal moment of inertia,  $I_{zz}$ , and equatorial ellipticity,  $\nu$ , emits a characteristic GW strain [Bonazzola & Gourgoulhon (1996)] that can be estimated from the energy emission rate  $L_{GW}$  given as  $L_{GW} \sim \frac{G}{c^5} \epsilon I_{zz}^2 \nu^6$  and rewriting in terms of Schwarzschild radius  $R_s = 2 \frac{GM}{c^2}$  and the rotation velocity  $V = 2\pi R \nu$  at the surface of the star  $L_{GW} \sim \frac{c^5}{G} \epsilon \left(\frac{R_s}{R}\right)^2 \left(\frac{V}{c}\right)^2$ .

### 2.3. Neutron star-blackhole

Astrophysical compact binary systems of neutron stars black holes (NSBH) mergers have firmly established themselves as prime sources for multimessenger astronomy, holding a strong electromagnetic counterpart. NSBH systems are also of curiosity in an astrophysical sense because they would allow studying the behavior of compact objects in strong-field regime the merger phase would provide important figures about the tidal disruption of NS and their equation of state. Since the noise signals restrain the original signal, the around  $\sim 250,000$  templates have been generated. We have thereby discussed the waveform families that have been used in the model. Unlike binary neutron stars, GWs from NSBH binaries will incorporate the GW signatures of the interaction between the BH. The most common class of waveforms that have been used in works of Kumar et al. (2015) and have been employed in our data are: PN approximation and Effective One Body (EOB) approximation. The description of the waveforms templates that have been used during the data generation scheme has been discussed in Sec-4.1, implemented using LALSuite Simulations.

### 2.4. Gravitational wave echoes

All the Black-hole (BH) merger ringdown events that have been detected until now are compatible with the known laws of General Relativity. However, (Cardoso et al. 2016a), in their recent work, has shown that the ringdown part can be used as a probe to study compact objects' structure. A very compact object smaller than that of a BH with a proton-sphere will also exhibit similar ringdown features as that of a BH. These objects are called Exotic Compact objects (ECO).

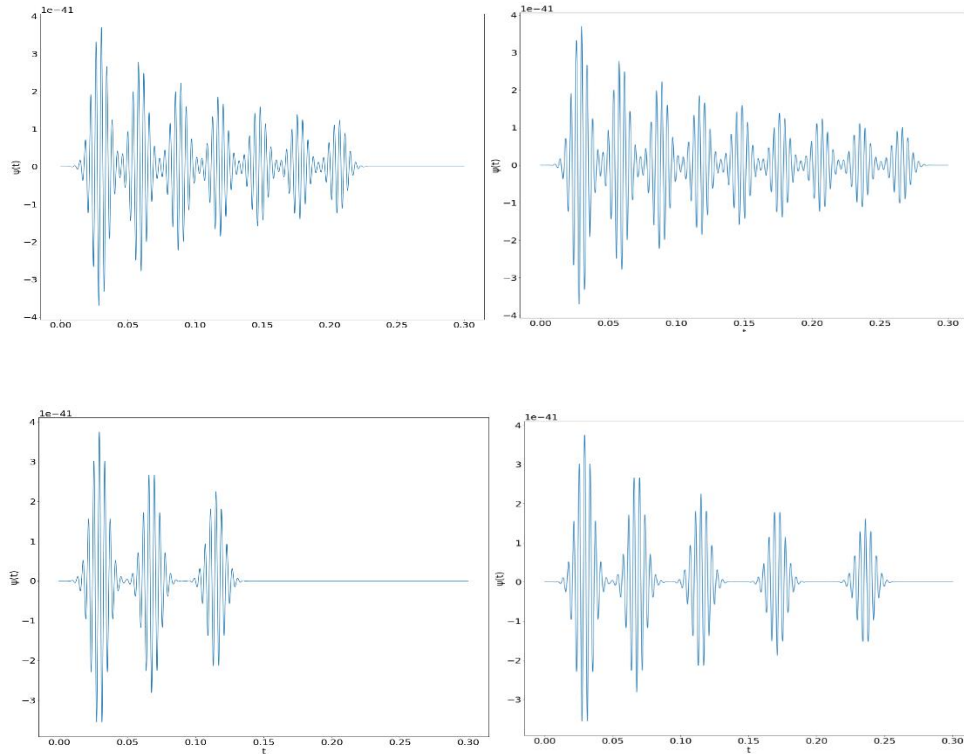


FIG 1. GW echoes waveform templates of amplitude strain vs. observation time. Upper section depicts CIE waveform template and the lower section UIE waveform template.

Initial ringdown signals, such as those observed by the LIGO detector, reflects only the geometry near the photon sphere and is thereby presumed to be very comparable to that of a GR black hole if the surface of the ECO is deep inside the photon sphere [Cardoso et al. \(2016a\)](#). GWs, specifically the echoes, reflected by the ECO's surface, are expected to show up only in the GW signals at a later stage. Thus, their detection will be prime evidence of ECOs. Physically, echoes in the late-time ringdown signal are caused by repeated damped reflections between the ECO's surface and the potential barrier at the photosphere. The time interval between the two successive echoes governs the system's fundamental physics, and it also leads to sub-classification of the echoes on the ground whether the echoes are at a uniform repeated interval or different interval.

We have employed a basic phenomenological approach towards the generation of waveform template, as mentioned in [Wang et al. \(2019\)](#). This is undoubtedly not the only technique for the development of the waveform template, and other successful methods have been employed for the same which can be seen from [Abedi et al. \(2017\)](#), [Lo & Weinstein \(2017\)](#) keeping the phase such that each successive echo will be in opposite phase due to the reflection from an ECO surface, Fig-2 (Left). We thereby follow with the description of the parameters used in the waveform

$$\Psi(t) = \Psi_{BH}(t) + \Psi_{echo}(t)$$

$$\Psi(t) = Ae^{\frac{t}{\tau}} \cos(2ft + \Phi) + \sum_{n=1}^{\tilde{N}_{echo}} (-1)^n A_n e^{-\frac{x_n^2}{2\beta_n^2}} \cos(2\pi f_n x_n) \quad (7)$$

Where  $\Psi_{BH}(t)$  is the post-merger - ringdown phase waveform having amplitude  $A$ , damping time  $\tau$ , reference phase  $\Phi$ , and central frequency  $f$ .  $\Psi_{echo}(t)$  is the waveform for the echo where the parameter description is as follows:  $\tilde{N}$  is the number of echoes post-merger phase,  $\beta_n \sim \beta$  to maintain the Gaussianity of the waveform and  $A_n \sim \frac{\Lambda A}{3+n}$  and  $\Lambda$  is the ratio of the amplitude of the first echo relative to  $A$ .  $f_n \sim f$ . Now since the time interval between the echoes can be differentiated based on being equal or unequal thus the form of  $x_n$  is different for the constant interval echo (CIE, Eq-9) and unequal interval echo (UIE, Eq-10) templates

$$x_n = t - t_{echo} - n\Delta t_{echo} \quad (8)$$

wherein  $\Delta t_{echo}$  - constant time interval between two successive echoes and  $t_{echo}$  is time interval between the main merger signal and the first echo.

$$x_n = t - t_{echo} - \frac{n(n+1)}{2} r \Delta t_{echo} \quad (9)$$

$\Delta t_{echo}$ :  $\delta t = r \Delta t_{echo}$  with  $r$  being constant.  $r \Delta t_{echo}$  term is due to the dynamical characteristic of the ECO surface. We choose  $\tau = 4 \times 10^{-3}s$ ,  $f = 250Hz$ ,  $\phi = 0$ ,  $A = 1.5 \times 10^{-21}$ ,  $\Lambda = 0.5$ ,  $\beta = 0.006s$ ,  $\Delta t_{echo} = 0.0295s$ ,  $r = 0.15$ , and  $t_{echo} = 0.0295s$  as explained in [Cardoso et al. \(2016b\)](#). Fig-1 shows examples of the above CIE and UIE waveform templates generated using the aforementioned equations.

## 2.5 Core-collapse supernovae

Core-collapse supernovae (CCSNe) events radiate massive radiation energies in the form of GWs that marks the violent death of massive stars having masses  $\sim 8M_{\odot}$ . This collapse will trigger a supernova explosion if the star's mass is  $<40M_{\odot}$ -  $50M_{\odot}$ , [Scheidegger \(2011\)](#) resulting in the formation of Types **II** and  $I_b/I_c$  supernovae. The Type  $I_b/I_c$  deviates from Type **II** due to the absence of hydrogen from the H-spectra, having an absence of Balmer lines marking the absence or the low evidence of Si and strong presence of He in Ib(details in [70-90] citations of [Abbott et al. \(2016b\)](#)).

The phenomenon begins with forming the iron core within, resulting in steady growth due to silicon burning. The star's inner part though hot but the soaring densities and the ordered arrangement of its constituting nucleons ends in a low specific entropy. Once the mass of the iron core exceeds Chandrasekhar mass limit, the electron degeneracy pressure cannot support the core pressure, resulting in the core collapse. At the given densities and temperature, additional phenomenon that robs the core's energy and pressure support are a) electron capture and b) photo-dissociation.

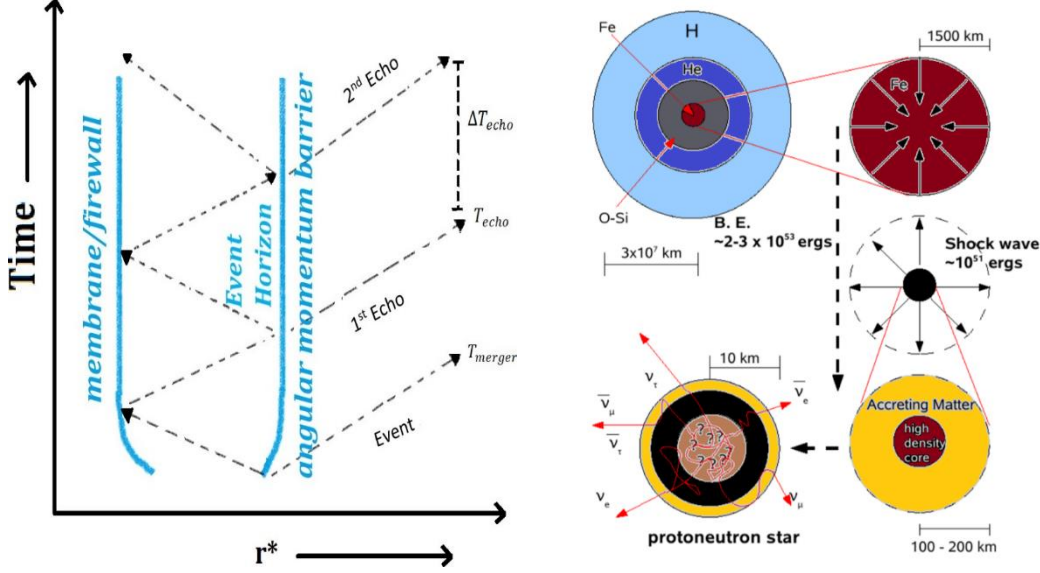


FIG 2. Left: Spacetime displacement of GW echoes from a membrane on the stretched horizon, following a BH merger. Right: Depicts a sequence of making of a nascent neutron star from the collapse of a stellar core. Beginning with a massive star with an 'onion-skin' structure, it goes through core implosion. The core bounces back, and shock waves are generated, resulting in a proto-neutron-star stage before the explosion, and then the isolated neutron star starts cooling after the explosion has occurred. The mass motion is depicted by the black and straight arrows, whereas curved red arrows show the escaping neutrons. Binding energy is depicted by B.E., and '?' denotes the (proto) neutron star's structure and composition, which is not fully understood.

Electron capture leads to a significant reduction in  $Y_e$ , and photo-dissociation leads to a further reduction in the temperature, consequently resulting in a drop of pressure support. The more massive the core, the higher shall be the phenomenon. The inward collapse of the core is restricted by nuclear forces when its interior density,  $\rho_c$  is 2–10 times the nuclear density. This abrupt halt of the collapse results in the rebound, generating a hydrodynamic shock wave resulting in core overshooting the equilibrium position and leading to the back and forth bounce, deviating about its mean radius. Once the supersonic inward falling material hits the rebounding inner core hydrodynamic shock waves are generated. If the inner core pushes the shock outwards with energy  $E > 10^{51}$  ergs, then the remainder of the star can be ejected in about 20 MS Scheidegger (2011) which is called prompt explosion. However, these hydrodynamic shock waves (Prompt explosion) will not lead to the explosion; thereby, it has to be revived. Following the core bounce, a dense remnant begins to form at the collapsing star's center, growing through the stellar material falling in. This newly formed remnant – proto-neutron-star (PNS).

Radiation will be radiated during the collapse/explosion due to the changing quadrupole moment  $L_{ij}$ . For finding numerical solutions and computation of GWs due to CCSNe, Fryer et al. (2002) used quadrupole approximation valid for nearly Newtonian sources Misner et al. (1973). The reduced  $L_{ij}$  of the source can be expressed as:  $L_{ij} = \int \rho (x_i x_j - \frac{1}{3} \delta_{ij} r^2) d^3 r$  where  $i, j \in \{1, 2, 3\}$  are spatial indices and  $r = \sqrt{x^2 + y^2 + z^2}$  denotes the distance to the source.  $h_x$  and  $h_+$ : the two polarizations of the GW field, can be evaluated in terms of  $L_{ij}$ . The maximum value of the RMS strain as from Dimmelmeier et al. (2001) can be evaluated as  $\sqrt{\langle (h_+^2) \rangle + \langle (h_x^2) \rangle}$ , where  $\langle \rangle$  indicate that averages taken over wavelength and angle of view at the sky. Corresponding to the  $A^{E2}$  quadrupole amplitude,  $\theta$  corresponding to the angle of view, the GW strain can be calculated using Thorne (1980).

$$h_+ = \frac{1}{8} \sqrt{\frac{15 A_{20}^{E2}}{\pi r}} \sin^2 \theta \quad (10)$$

We have generated a template bank using pre-simulated data that contains a set of 26 rotational supernova core collapse models [https://www.mpa-garching.mpg.de/rel\\_hydro/axi\\_core\\_collapse/index.shtml](https://www.mpa-garching.mpg.de/rel_hydro/axi_core_collapse/index.shtml) in axisymmetric. Sec-4.1.4 discussed the pipeline used for the dataset generation using the aforementioned model.

## 2.6 Non-gaussian random noise

The interferometers measure the strain values to a very high order of accuracy up to  $10^{-21}$ m. The low interacting nature of the GWs makes it impossible to be detected easily by any known matter; the sensitivity of the interferometer is justified. Efforts had been made to keep the interferometer as quiet as possible (i.e., away from all the possible noises that can be induced in the signal leading to disruptive signal quality and further computational process to filter the signal). Despite the intellectual efforts made to insulate the interferometer from the environmental noises completely, somehow, the noises tend to leak in the signal, adding a series of signal processing methods like bandpass filtering, notching to obtain the waveform that shows a strong probability of being a GW candidate. The interferometer's strain value sensitivity to astrophysical events capable of producing detectable signals is affected by fundamental noise sources such as thermal noise tracing out from the test masses and their suspension systems; quantum noise comprises shot noise at high frequencies, technical noise sources, which can be controlled by the design of the detector. Several significant upgrades were executed between successive runs to reduce these noise sources e.g., noise source from air compressors (a specific glitch discussed in Sec-2.6), paddings were used to reduce the instrument vibrations, and hence data after 26<sup>th</sup> Sept 2016 had no trace of AC glitches thereby improve the detectors' sensitivities towards the true signal. Introduction of larger and heavier test masses have been very effective in diminishing the thermal noise and motion induced by quantum radiation pressure.

Thus, the environmental noise is a combination of various classes: quantum sensing noise, seismic noise, suspension thermal noise, and gravity gradient noise, which have a Non-Gaussian nature. Also, the transient noise events: anthropogenic sources, weather, equipment malfunctions, and occasional transient noise of unknown origin also superimpose the classes mentioned above. Thus, the signal has to undergo a series of signal processing, vetoing the unwanted frequencies that affect the true signal, adding to a computational cost and time. [Nuttall et al. (2015a)-Nuttall et al. (2015b)].

## 2.7 Glitches

Transient Non-Gaussian noises that have a significant characteristic, known colloquially as glitches as discussed above. Glitches are usually technical or hardware noise that trickle into the detector. Although along with the channel for detection of GW, 200,000 auxiliary channels have been created that monitor the surrounding, environmental conditions, and the interferometer's hardware. These channels are critical and play a key role - primarily to find the cause of the noise source by recording the surrounding conditions prevailing during the detector run [Effler et al. \(2015\)](#). These non-cosmic disturbances (glitches) have a feature of masking the true signal, leading to false alarms and increased signal rate than the true rate. Extensive work has been done to detect the unknown glitches and their sources, employing novel methodology to if not completely eradicate, then to minimize the effect as far as possible. One of the best examples is the Gravity Spy project [Zevin et al. \(2017\)](#), which is in effort to classify the glitches that occur in the signal into classes that are defined on the ground of features that are comprehensible to human vision. This project is a classic example of how well we can combine the power of Citizen Science as well as using Machine Learning (ML) Algorithm to solve critical and challenging problems.

So far, 22 classes of glitches have been classified based on their known features and appearances, as extracted by ML algorithm. Examining the results of work by [Bahaadini et al. \(2018\)](#), some classes are sparsely populated, but a few tend to overlap, which is justified by the closeness in the frequency range and similarity power and appearance. Fig-3, in their work, justifies the aforementioned statement. There are certain classes of glitches that have a higher rate of occurring than the others e.g., the glitch due to the phone ringing, raven crossing, noise due to aircraft or other such events have a lesser probability though have enough power to disturb the signal. We have taken 18 class of glitches from amongst the 22 classes of glitches labeled in works of [Bahaadini et al. \(2018\)](#). The classes that we have taken into account for our analysis are mentioned in table-1 with a brief description describing the characteristic features used for classification and generating the signal.

## 3. PREVIOUS WORKS

In this section, we shall discuss the previously established novel methods that have been employed for the classification of astrophysical signals. Astrophysical signals have usually superimposed with various noise forms that have to be removed for the study, which can be done by either preparing a set of a pre-simulated dataset and then matching the filtered signal and then studying the properties corresponding to the synthetically produced dataset - match filtering method, which is time-consuming and computationally cumbersome [[Raman \(2017\)](#)]. The introduction of DL in the field of astronomy was primarily employed by [Carleo et al.](#) Since then, many DL models have been developed, and with advancing computational power, the primary task of classification of astronomical data from the noise has been achieved to very high accuracy.

Since the introduction of the Machine Learning technique in astronomy, many models have been proposed using different classification methods with very high accuracy as in [Zevin et al. \(2017\)](#) and [Bahaadini et al. \(2018\)](#). In the above example, the

classification of Glitches by Gravity spy project is a stark example of how efficiently and accurately the classification can be accomplished. There have been several occasions where employing ML techniques has proved far better regarding computational cost compared to DL. However, DL models having a structured arrangement of layers (discussion Sec-4.2) having several neurons that triggers only after some activation threshold, making it much more efficient in feature extraction. DL-CNN method is an acute method for classification problems and has been successfully employed for various other classification domains. The classification done by Razzano & Cuoco (2018) and Gebhard et al. (2019) shows how efficiently the signal classification can be done. Moreover, CNNs have shown high accuracy when predicting a given dataset’s multiple features, such as predicting emotion and movie genre prediction. In our work, we have also used a similar approach, a multi-label classification model for predicting properties of GWs if detected.

TABLE 1. Classes of glitches used and the corresponding features under which classification has been done

Class	Frequency Range (Hz)	Duration	Evolving
1080 Lines	~1080	Long	No
1400 Ripples	~1400	Short	No
Air Compressor	50-60	Short	No
Blip	30-500	Short	Yes
Chirp	30-500	Short	Yes
Helix	30-500	Short	Yes
Koi Fish	30-500	Short	Yes
Light Modulations	30-200 (sharp spikes)	Long	Yes
Paired Dove	5-150	Short	Yes
Power Line	~60	Short	No
Repeating Blips	30-500	Short	No
Scattered Light	20-60	Long	Yes
Scratchy	30-300	Long	Yes
Violin Mode	~500	Short	No
Tomte	30-300	Short	Yes
Whistle	>300	Short	Yes
Wandering Lines	>1000	Long	Yes

## 4. METHODOLOGY

This section is separated into three subsections: Data generation, Model selection, testing, and data validation. In each subsection, we have followed the same order: discussing the methodology used for data generation, the reason, and justification. Firstly, we discuss the importance of the carrier wave/ background data and the specific characteristics that have been used for the model, preserving the physics of the real world.

### 4.1. Dataset generation

In the proceeding subsections, we have discussed the data generation scheme. In reality, most detection events are expected to be faint due to the extreme distance between the detector and the event source, specifically the GW events. Focusing on the GW events and assuming them to have an isotropic distribution throughout the sky, more than 50% of the data will be above the detectible sensitivity. Thus, there will hardly be any detections, as a more significant fraction of signals will be even close to the verge of detection, making the DL model harder to operate and predict accurately. A common approach of *curriculum learning* Bengio et al. (2009) has been used while training the model, which is the approach of first training the model with easier datasets and then moving on to the difficult datasets. Each data component previously discussed in Sec-2 has been synthetically injected primarily as an individual class to the background wave. Moreover, maintaining the data’s physical reality and ensuring that the model works efficiently in the real-time combination of individual trigger events’ (BH binaries, NS binaries, CCSNe) combination of the same synthetic data has been injected randomly in the sample background wave. A complete pipeline for the data generation can be summarized from Fig-4. For this work, we have created a dataset with time-series signals of 12s data. Partition has been done for training, testing, and validating into 70%, 20%, and 10% respectively of the data generated. Several examples not containing any injections are generated by simply skipping the injection step so that the model maintains physical reality as far as possible. We

generated four times as many examples that contain an injection than a noise sample.

#### 4.1.1. Background data/ carrier wave

The fundamental idea employed for the time-series data generated is that the LIGO data is the superimposition of various waveforms, and those once decomposed, individually represent a waveform as per the wave superposition law. We have assumed LIGO random Non-Gaussian noise to be the carrier wave/background signal over previously discussed class of signals gets superimposed. We have used real LIGO O1 and O2 data, keeping in mind the following key features:

- The signal should not have any real detection signal and must only contain non-Gaussian transient noise.
- The signal is sampled out must be free from any glitch signal as far as possible since some of the glitches as discussed from table-1 are of long duration and non-evolving, for example, 1080 Lines and 1440 Ripples.
- Both the detectors should be functional.
- We excluded all time segments having hardware injections.

#### 4.1.2 Blackhole binaries and neutron star binaries

The basic procedure of developing simulated synthetic waveform template bank for BH binaries and NS binaries has been discussed in Sec-2.1. This set of trigger events was generated using the PyCBC pipeline. The LALSuite simulations return two polarization modes, namely  $h_x$  and  $h_+$ . PyCBC provides routines for calculating these polarized strain values. The table-2 below summarizes the parameters that we have used to produce a template bank of the desired SNR.

TABLE 2. Data generation parameters for BHB and NSB

Approximants	Mass1 ( $M_\odot$ )	Mass2 ( $M_\odot$ )	Distance (Mpc)	Lower freq(Hz)	Upper freq(Hz)
TaylorT1	5-15	5-15	50-450	60,120	50
TaylorT2	5-15	5-15	50-450	60,120	50
EOBNRv2	5-15	5-15	50-450	60,120	50
SEOBNRv2	5-15	5-15	50-450	60,120	50

#### 4.1.3 GW echoes

GW echoes were simulated using basic mathematical routines, as discussed in Sec-2.3. The model parameters that were altered to produce a template bank are mentioned in the table along with the variations for CIE and UIE waveform, respectively. The table-3 summarizes the parameters on which waveform templates have been generated.

TABLE 3. Data generation parameters for GW echoes

Parameters	CIE	UIE
$\Lambda$	(0, 1)	(0, 1)
$\beta$	(0.001, 0.01)	(0.001, 0.01)
$t_{echo}$	(0.02, 0.04)	(0.02, 0.04)
$r$	NA	(0.1, 0.2)
$\Delta t_{echo}$	(0.02, 0.04)	(0.02, 0.04)

#### 4.1.4 Core collapse supernova explosion

We have generated a template bank using pre-simulated data containing 26 rotational supernova core-collapse models [https://wwwmpa.mpa-garching.mpg.de/rel\\_hydro/axi-core\\_collapse/](https://wwwmpa.mpa-garching.mpg.de/rel_hydro/axi-core_collapse/). The data obtained encapsulated time-series evolution of  $A^{E20}$ . The data was converted to strain time-series signals using the Eq-11, the angle of view varying at  $30^\circ$  and  $90^\circ$  and distance from 10 Mpc to 30 Mpc. Table-4 that corresponds to the data parameters and conditions under which the waveform has been generated. (See Appendix Fig-9)

#### 4.1.5 Glitches

Since using a DL model that extracts features from the time-series strain value,  $h(t)$ , hence spectrograms were primarily converted to time-series data. We generated short signals, as mentioned in table-1 from a methodology of Image to sound mapping, wherein every image having color components as RGB or grayscale can be transformed into respective sound. The short duration glitches

are harder to detect in the framed sample, and few are shorter than a second. Fig-3 illustrates the conversion procedure of a three grey-tone image having dimensions  $8 \times 8$ . This mapping translates for individual pixel, vertical position into frequency, horizontal position into time-after-click, and brightness into amplitude, which is the power in any spectrogram. For every column, each column's pixel is used to excite a similar sinusoidal wave in the audible frequency range.

TABLE 4. Data parameters for Core collapse Supernovae

Model	$ A_{20max}^{E2} $	$d A_{20max}^{E2} $	Type
A1B1G1 <sup>R</sup>	950	-44	I
A1B2G1 <sup>R</sup>	1795	-23	I
A1B3G1 <sup>R</sup>	2694	+84	I
A1B3G2 <sup>R</sup>	1723	-17	I
A1B3G3 <sup>R</sup>	663	-17	I
A1B3G5 <sup>R</sup>	950	-32	I
A2B4G1 <sup>R</sup>	124	-5	III
A3B1G1 <sup>R</sup>	522	-20	I
A3B2G1 <sup>R</sup>	950	-44	I
A3B2G2 <sup>R</sup>	950	-44	I
A3B2G4 <sup>R</sup>	950	-44	I
A3B2G4 <sup>R</sup>	506	-28	I
A3B3G1 <sup>R</sup>	1035	-5	II
A3B3G2 <sup>R</sup>	1305	-8	I/II
A3B3G3 <sup>R</sup>	1255	-15	I/II
A3B3G5 <sup>R</sup>	256	-3	III
A3B4G2 <sup>R</sup>	624	-30	II
A3B5G4 <sup>R</sup>	491	-7	III
A4B1G1 <sup>R</sup>	2325	+17	I
A4B1G2 <sup>R</sup>	2003	-2	I
A4B2G2 <sup>R</sup>	3026	+42	I/II
A4B2G3 <sup>R</sup>	2209	-4	I/II
A4B4G4 <sup>R</sup>	925	-47	I/II
A4B4G5 <sup>R</sup>	1212	-44	I/II
A4B5G4 <sup>R</sup>	1828	-38	I/II
A4B5G5 <sup>R</sup>	2629	-31	I/II

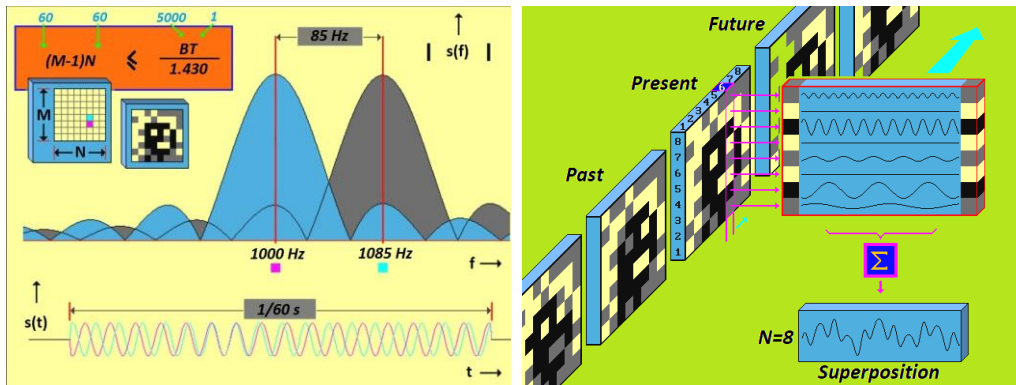


FIG 3. In order to achieve a high resolution, each image is transformed into a time-multiplexed auditory representation.

The simplest form results in a spectrogram synthesis where every pixel is mapped to a brief pure tone of a specific frequency and amplitude corresponding to the power (brightness) of that pixel. However, a pure tone of less than infinite duration (theoretically) does not give a perfect spectral line but evaluates a spectral envelope with the main lobe and side lobes. Thereon the spectral envelope will

overlap known as spectral leakage. Thus, the shorter duration sounds will have a greater spread of frequency, limiting the sufficient resolution in spectrogram-like mappings, resulting in a signal that is not usually the pure sound signal and has some random noise that needs processing before injecting into the background wave. To filter the signal to obtain the true glitch signal, we used a method `scipy.signal.filtfilt` from the python SciPy Python package. This function applies a linear digital filter twice, once forward and once backward. The combined filter has zero phase and a filter order twice that of the original (<https://docs.scipy.org/doc/scipy/reference/generated/scipy.signal.filtfilt.html>). Thus time-series signal of the glitches as mentioned in table-1: ac, helix, koi fish, light modulation, low frequency burst, paired dove, repeating blip, scattered light, Tomte, scratchy, whistle, wandering line, were generated using this method. Fig-8 (Appendix) shows the time-series glitch signals that were injected into the carrier wave using this method.

#### 4.1.6 Random injection of data

This part of the dataset has been introduced purposely to ensure that the synthetically generated data resembles real-world data, ensuring that the model is trained to classify any interferometric time-series strain data in real-time successfully. The different synthetic data classes that have been generated are injected into the background wave containing trigger events- BHB, NSB, NSBH, and CCSNe individually, and thereon randomly injecting glitches. The random injection ensures that the signal does not occupy the central vector space and is sparse, as is the real data. There are two sets of mixed signals: Mix of binaries: having random injections of BHB, NSB, NSBH, GW echoes, Mix of CCSNe: CCSNe and Glitches. The following figure illustrates the complete data generation pipeline for our model-

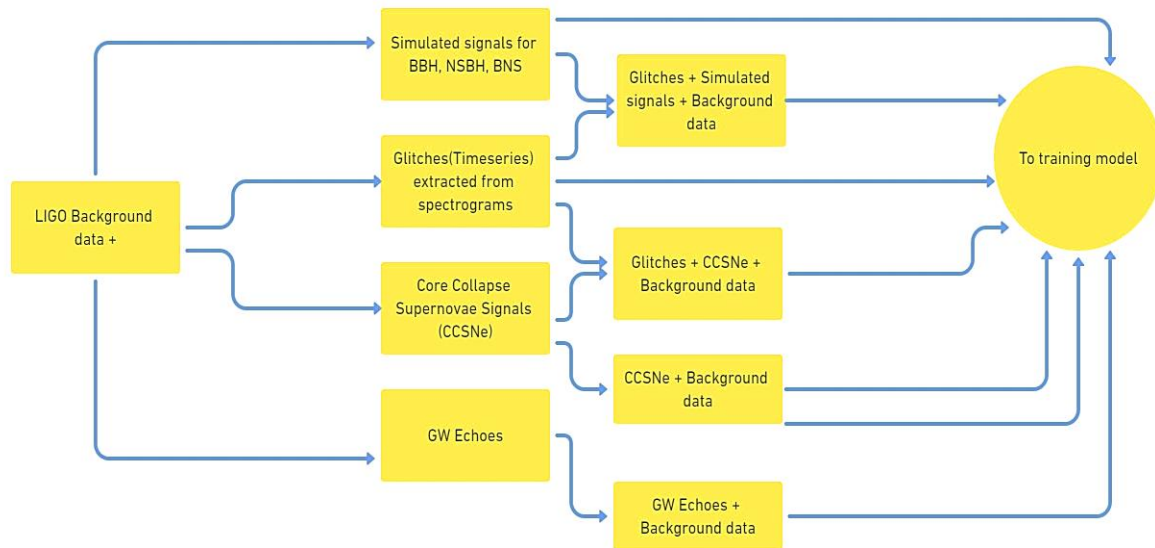


FIG 4. The complete data generation pipeline for feeding the CNN model

#### 4.2. Model selection

We chose Convolutional Neural Network (CNN) as the model due to the dataset's nature: time-series data having 16,384 data points with 27 features to be extracted. Compared to its predecessors, CNN's ability is that it automatically detects the essential features without any human supervision. DL models having a structured arrangement of layers (discussion Sec-4.2) having several neurons that triggers only after some activation threshold, making it much more efficient in feature extraction. Overfitting and large data requirements have been significant issues, but with further advancement and development of a new model, e.g., Deep Transfer Learning needs not to be fed with excessive data every time it is trained and works fine with a smaller dataset due to its ability to reutilize the previously trained knowledge. RNN's have LSTM used to train time-series data, a memory unit that enables the network to remember the previously trained dataset and process and predict the sample data using the previous knowledge. CNN based models have been previously used for several tasks: Natural Language Processing (NLP), Image classification, Glitch classification, GWs searches as well [Zevin et al. (2017), Bahaadini et al. (2018), Gebhard et al. (2019)]. As mentioned earlier, CNN's have performed extremely well on binary classifications; however, earlier from Wang et al. (2016) and works in biomedical areas Farooq et al. (2017) indicates the ability to perform on a similar level for a multi-classification problem.

### 4.3. Model architecture

Our CNN network architecture is 29 layers deep with 13 Convolutional layers (CNL), 13 Dropout layers, 1 Flatten layer, and 2 Dense layers. We defined a nonlinear activation function after each convolutional layer, ReLU, followed by a dropout layer. We used the dropout parameter 0.3, restricting 30% of neurons. Finally, we used 2 Dense Layers with ReLU and Sigmoid, respectively. We had conducted a training experiment on the whole data set 10 times corresponding to each varying-parameter listed below. The results obtained on altering various parameters can be summarized from Fig-6.

- learning rate:  $10^{-1}, 10^{-2}, 10^{-3}$
- batch size: **100, 200, 250, 500**
- Kernel Size: **2, 3, 4**

Finally from the summary of Appendix Fig-6 and Appendix Fig-7 we chose our network architecture as mentioned in Table-5.

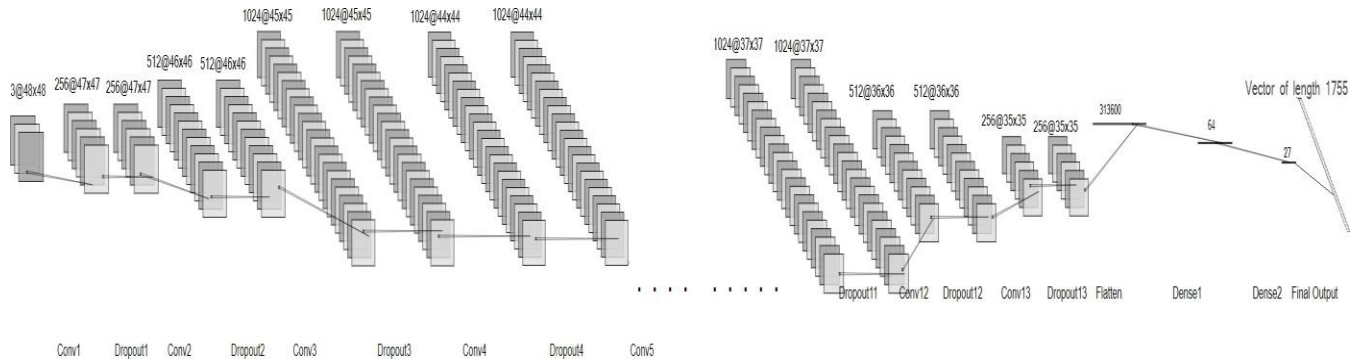


FIG 5. Model architecture

During the first convolution, the input signal having a single channel that has already been converted to the data of shape (48,48,3) will primarily be convoluted by the 256 filters having kernel size as (3,3) and translating 1 step at a time. The architecture grows and widens to 1024 layers from 256 to 512 and then to 1024, and then narrows down to 256 filters at the last CNL. A Flatten layer follows this, and finally, we have two dense layers giving the outputs (64,1,1) and (27,1,1), respectively. Finally, the model yields a vector of size 1755. The output 1D network output is then passed through a sigmoid layer, mapping it within the interval (0,1). This method yields a relatively large receptive field for 12s data with a depth of 13 CNL blocks. However, memory limitations during training upper-bounded the number of channels to 1024. This implementation has been done in (in PYTHON 3.6.7) is based on the KERAS deep learning framework [Chollet et al. \(2015\)](#). A schematic model architecture is depicted in Fig-5

### 4.4. Model training

As mentioned above, the method of curriculum learning has been used to train the model. During training, the performance was regulated by continually estimating the model on the validation set. During training, the kernel entries are optimized by Stochastic Gradient descent (with momentum 0.95) having a learning rate of  $10^{-3}$  and decay  $10^{-6}$ . With every epoch, the dataset is randomly shuffled and divided into batches of batch size 500. Binary Cross-Entropy (BCE) has been used, calculated batch-wise at every time step. This calculated batch loss gradient is evaluated for all kernels, and error back-propagation is used to twitch the kernel values towards converging solution. At the end of every epoch, the network's performance with its current parameter values is evaluated both on the full training and validation data set. The model's training was done on a Portable machine with Intel Core -i7 7700 HQ processor (base clock 2.8 GHz and boost clock 3.6 GHz), NVIDIA GTX 1060 6 GB graphics, with 16 GB RAM and took approximately 40 hours to train for 30 epochs. On further training, the model's training accuracy marginally increased, but the validation accuracy and testing accuracy decreased, indicating over-fitting.

TABLE 5. CNN model summary

Layer	Input Shape	Output Shape	kernel size	stride	padding	Activation
Convolution <sup>1</sup>	(48,48,3)	(47,47,256)	(3,3)	1	2	ReLU
Dropout <sup>1</sup>	(47,47,256)	(47,47,256)	-	-	-	-

Convolution <sup>2</sup>	(47,47,256)	(46,46,512)	(3,3)	1	2	ReLU
Dropout <sup>2</sup>	(46,46,512)	(46,46,512)	-	-	-	-
Convolution <sup>3</sup>	(46,46,512)	(45,45,1024)	(3,3)	1	2	ReLU
Dropout <sup>3</sup>	(45,45,1024)	(45,45,1024)	-	-	-	-
Convolution <sup>4</sup>	(45,45,1024)	(44,44,1024)	(3,3)	1	2	ReLU
Dropout <sup>4</sup>	(44,44,1024)	(44,44,1024)	-	-	-	-
Convolution <sup>5</sup>	(44,44,1024)	(43,43,1024)	(3,3)	1	2	ReLU
...	...	...	...	...	...	...
...	...	...	...	...	...	...
...	...	...	...	...	...	...
Dropout <sup>11</sup>	(37,37,1024)	(37,37,1024)	-	-	-	-
Convolution <sup>1</sup> <sub>2</sub>	(37,37,1024)	(36,36,512)	(3,3)	1	2	ReLU
Dropout <sup>12</sup>	(36,36,512)	(36,36,512)	-	-	-	-
Convolution <sup>1</sup> <sub>3</sub>	(36,36,512)	(35,35,256)	(3,3)	1	2	ReLU
Dropout <sup>13</sup>	(35,35,256)	(35,35,256)	-	-	-	-
Flatten	(35,35,256)	(313600,1,1)	-	-	-	-
Dense <sup>1</sup>	(313600,1,1)	(64,1,1)	-	-	-	ReLU
Dense <sup>2</sup>	(64,1,1)	(27,1,1)	-	-	-	Sigmoid

## 5. PERFORMANCE METRICS

### 5.1 Label creation

In this section we shall discuss how we generated the labels, which is, the expected network output  $y$  for a given input time-series data  $x$ . For our network, it should be capable of not only predicting the presence of any GW signal but also predict its features from the noise time-series data. In the 27 features that network has to extract each of one was one-hot-encoded implying the value corresponding to any label class is either 0 or 1; 0 representing the absence of that class and 1 representing its presence.

### 5.2 Result Discussion

After 30+ hours of training, the model training accuracy, i.e., before the over-fitting was obtained between 89.97% and 90.1%, experimented for three times with the same model architecture. The validation accuracy was  $\sim 89.03\%$ , and validation loss was  $\sim 0.3\%$ . We tested the model accuracy on the 20% previously partition dataset, resulting in an accuracy of 89.93%. Fig-6 represents the parameters we altered during our experimentation and the maximum, which was achieved by the current architecture. During training, we observe an increase in training accuracy for odd-numbered kernel filter size and rising batch-size. Since we experimented with our model architecture with slightly lesser parameters, this result cannot be generalized yet. Moreover, case studies have shown a slight decrease in overall accuracy as the batch-size goes up.

## 6. CONCLUSION

In this work, we briefly introduced the methodology of synthetic preparation of data using NR for BH, NS, NSBH binaries, and CCSNe. We further investigated the GW Echoes and were able to synthetically inject the proposed two categories of the signal as in [Abedi et al. \(2017\)](#) as well as in [Lo & Weinstein \(2017\)](#). We also carried out an in-depth analysis of state-of-art deep CNNs for multiclass classification to classify the data during the running time of the detector itself. Firstly, we critically examined the existing classification methods opted and well tested, thereon attempting to extend classification problems towards multi-label classification. We use a simple but subtle network architecture tailored towards the multiclass classification of the real-time data generated by LIGO. The model does face accuracy loss due to scattered labels, a small dataset required for extraction of 27 features, slightly unbalanced data, and memory upper-bound. Thereby, we showcase a selection of failure modes of our model, typical for deep convolutional neural networks. While preparing the dataset for training, we infer that all injected inputs are physically possible. Future highly sensitive GW detectors could investigate the BBH, NSBH, BNS, CCSNe, and GW echoes and stochastic sources simultaneously, giving us an ameliorated picture of astrophysical phenomena in the observable universe. With the ever-escalating

template space of matched filtering, it would become increasingly challenging to de-noise the future GW signals without exponential computing performance. Deep learning models like ours could identify a plethora of different types of such signals much faster than Matched filtering, which would, in turn, allow for faster parameter estimation and aid in the localization of GWs for Multi-Messenger Astronomy. CNNs are an assuring tool for GW astronomy; however, their exact interpretation requires great care and attention, and one model which may work for a specific problem may not work for other challenges.

## ACKNOWLEDGMENT

We would like to thank Dr. Kamlesh N. Pathak, Professor, Applied Physics Department, whose constant guidance encouraged us to complete this project. We wish to show our gratitude to many people without whom this work would not have been complete. We would like to extend our special thanks to Mr. Ankul Prajapati, batch of 2020 graduate, Sardar Vallabhbhai National Institute of Technology, Surat, who motivated us to work in the field. This work has made use of data, software, or web tools obtained from the Gravitational Wave Open Science Center (<https://www.gwopenscience.org>), a service of LIGO Laboratory, the LIGO Scientific Collaboration and the Virgo Collaboration. LIGO is funded by the U.S. National Science Foundation.

## REFERENCES

- Abbott, B., Jawahar, S., Lockerbie, N., & Tokmakov, K. 2016a, *PHYSICAL REVIEW D* Phys Rev D, 93, 122003
- Abbott, B. P., Abbott, R., Abbott, T., et al. 2016b, *Physical Review D*, 94, 102001, 2016e, *Physical Review X*, 6, 041015
- Abbott, B. P., Abbott, R., Abbott, T. D., et al. 2016c, *Physical Review X*, 6, 041014, 2016f, *Physical Review D*, 93, 122003
- Abbott, B. P., Abbott, R., Abbott, T., et al. 2016d, *Physical review letters*, 116, 061102, 2018,
- Abedi, J., Dykaar, H., & Afshordi, N. 2017, *Physical Review D*, 96, 082004
- Abramovici, A., Althouse, W. E., Drever, R. W., et al. 1992, *science*, 256, 325
- Bahaadini, S., Noroozi, V., Rohani, N., et al. 2018, *Information Sciences*, 444, 172
- Baker, J. G., Boggs, W. D., Centrella, J., et al. 2008, *Physical Review D*, 78, 044046
- Bengio, Y., Louradour, J., Collobert, R., & Weston, J. 2009, in *Proceedings of the 26th annual international conference on machine learning*, 41–48
- Bernard F. Schutz, B. S. 2009, *Astrophysics and cosmology with gravitational waves*, *Classical and Quantum Gravity*, 35, 065010
- Blackman, J. L. 2017, PhD thesis, California Institute of Technology
- Blanchet, L., Buonanno, A., & Faye, G. 2012, arXiv preprint arXiv:1210.0764
- Bonazzola, S., & Gourgoulhon, E. 1996, arXiv preprint astro-ph/9602107
- Buskirk, D., & Hamilton, M. C. B. 2019, *European Journal of Physics*, 40, 025603
- Cardoso, V., Franzin, E., & Pani, P. 2016a, *Physical review letters*, 116, 171101
- Cardoso, V., Hopper, S., Macedo, C. F., Palenzuela, C., & Pani, P. 2016b, *Physical review D*, 94, 084031
- Chollet, F., et al. 2015, *Keras*, GitHub. <https://github.com/fchollet/keras>
- Damour, T., & Vilenkin, A. 2000, *Physical Review Letters*, 85, 3761
- Dimmelmeier, H., Font, J. A., & Müller, E. 2001, *The Astrophysical Journal Letters*, 560, L163
- Effler, A., Schofield, R., Frolov, V., et al. 2015, *Classical and Quantum Gravity*, 32, 035017
- Farooq, A., Anwar, S., Awais, M., & Rehman, S. 2017, in *2017 IEEE International Conference on Imaging systems and techniques (IST)*, IEEE, 1–6
- Fryer, C. L., Holz, D. E., & Hughes, S. A. 2002, *The Astrophysical Journal*, 565, 430
- Gebhard, T. D., Kilbertus, N., Harry, I., & Schölkopf, B. 2019, *Physical Review D*, 100, 063015
- Haskell, B., Samuelsson, L., Glampedakis, K., & Andersson, N. 2008, *Monthly Notices of the Royal Astronomical Society*, 385, 531
- Huerta, E., Kumar, P., Agarwal, B., et al. 2017a, *Physical Review D*, 95, 024038 2017b, *Physical Review D*, 95, 024038
- Kumar, P., Barkett, K., Bhagwat, S., et al. 2015, *Physical Review D*, 92, 102001
- Lo, R. K. L., & Weinstein, A. 2017
- Lousto, C. O., & Zlochower, Y. 2011a, *Physical review letters*, 106, 041101, 2011b, *Physical review letters*, 106, 041101
- Misner, C. W., Thorne, K. S., Wheeler, J. A., et al. 1973, *Gravitation* (Macmillan)
- Moenchmeyer, R., Schäfer, G., Müller, E., & Kates, R. 1991, *Astronomy and Astrophysics*, 246, 417
- Nuttall, L. K., Massinger, T., Areeda, J., et al. 2015a, *Classical and Quantum Gravity*, 32, 245005, 2015b, *Classical and Quantum*

Gravity, 32, 245005

Raman, A. 2017, arXiv preprint arXiv:1711.07421

Razzano, M., & Cuoco, E. 2018, Classical and Quantum Gravity, 35, 095016

Sathyaprakash, B. S., & Dhurandhar, S. 1991, Physical Review D, 44, 3819

Scheidegger, S. U. 2011, PhD thesis, University of Basel Szilágyi, B. 2014, International Journal of Modern Physics D, 23, 1430014

Thorne, K. S. 1980, Reviews of Modern Physics, 52, 299 Ushomirsky, G., Cutler, C., & Bildsten, L. 2000, Monthly Notices of the Royal Astronomical Society, 319, 902

Varma, V. V. S. 2019, PhD thesis, California Institute of Technology

Wang, J., Yang, Y., Mao, J., et al. 2016, in Proceedings of the IEEE conference on computer vision and pattern recognition, 22852294

Wang, Y.-T., Zhang, J., Zhou, S.-Y., & Piao, Y.-S. 2019, The European Physical Journal C, 79, 726

Weinberg, S. July 1972., Gravitation and Cosmology: Principles and Applications of the General Theory of Relativity (Wiley)

Woosley, S. E. 1989, Annu. Rev. Astron. Astrophys, 27, 629 Zevin, M., Coughlin, S., Bahaadini, S., et al. 2017, Classical and Quantum Gravity, 34, 064003



APPENDIXES

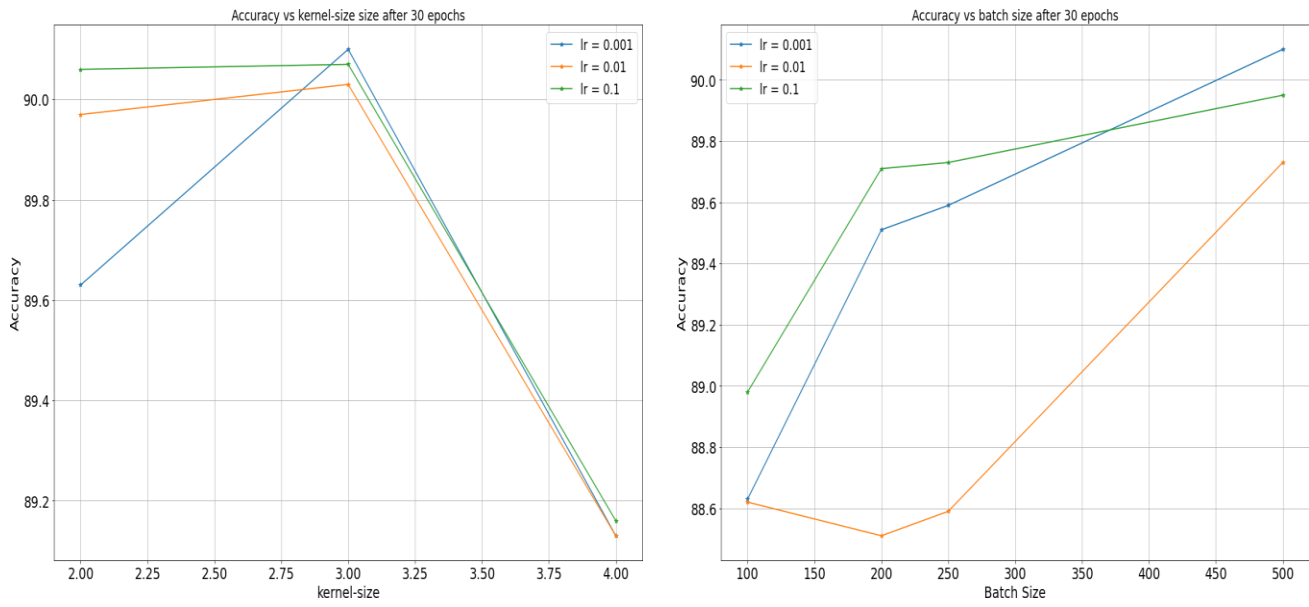


FIG 6. Parameters altered during training and their corresponding accuracy plots

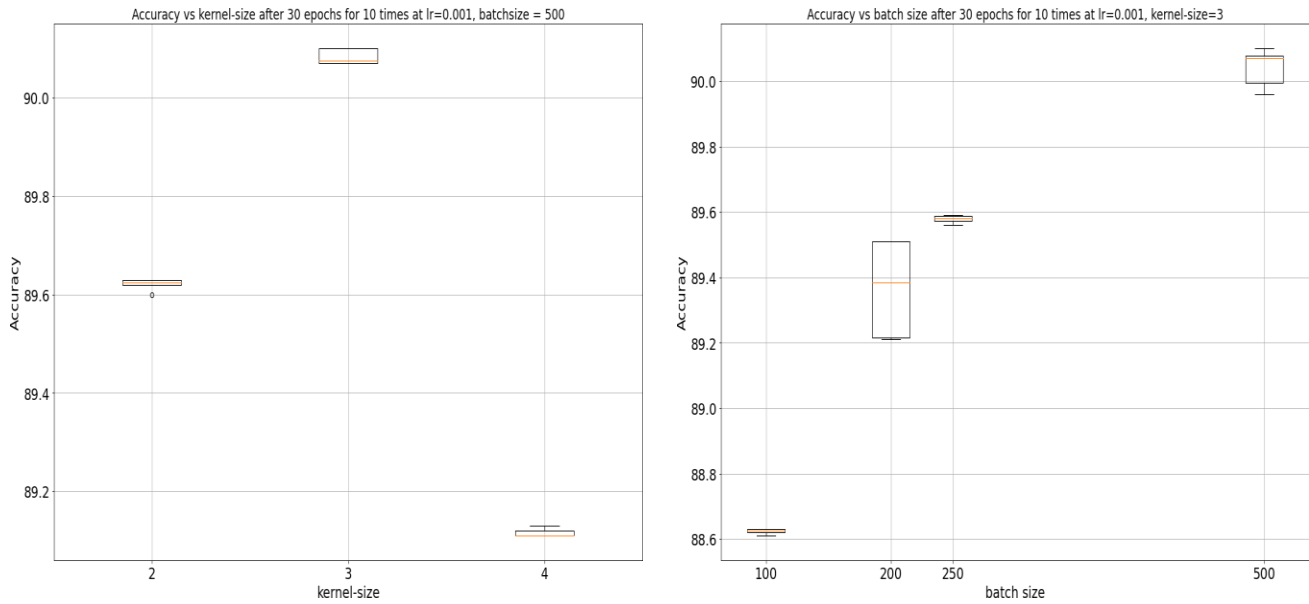


FIG 7. Accuracy variations for 30 epochs ran 10 times

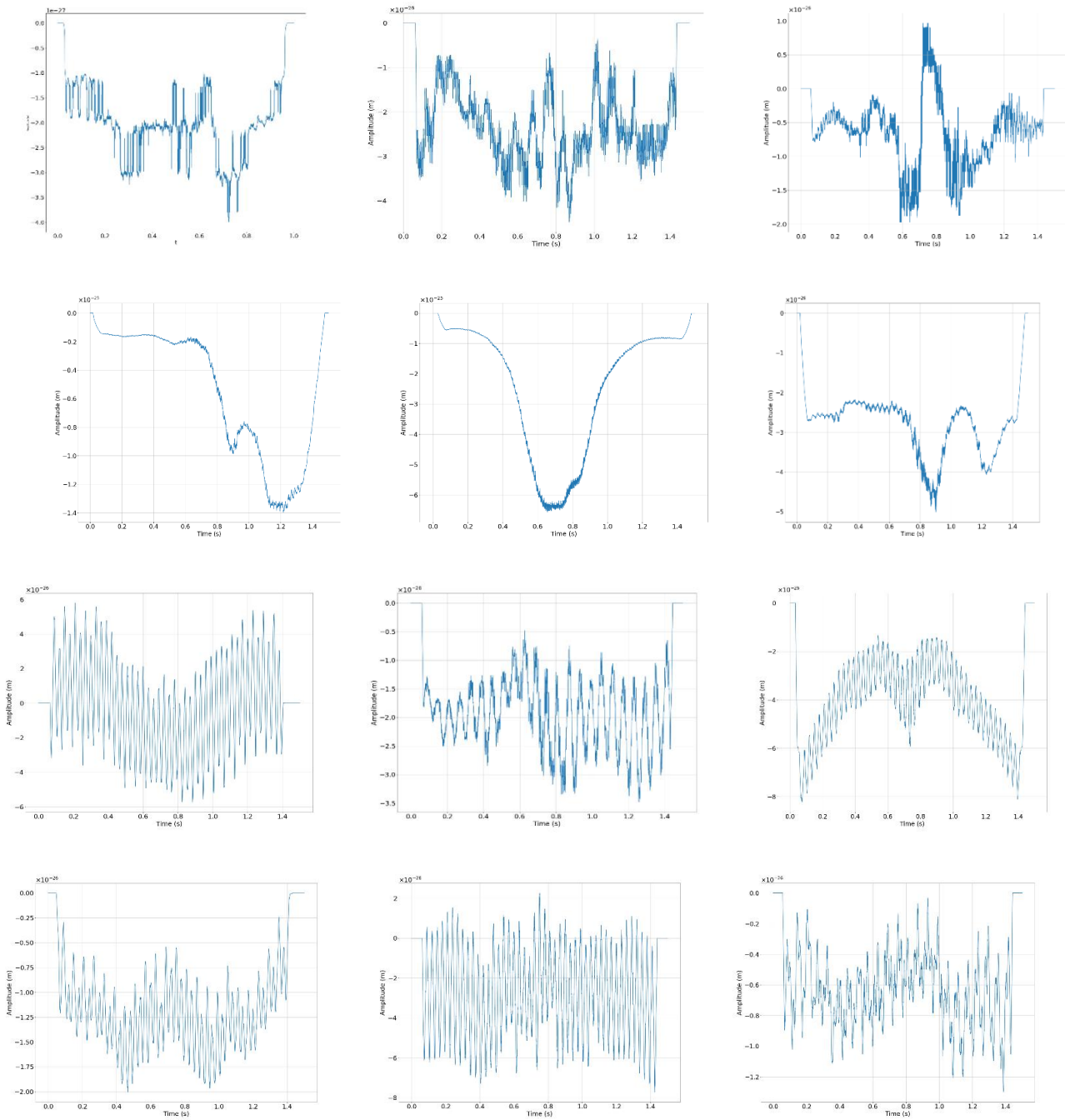


FIG-8. Waveform of the various glitches obtained from **Image to Sound** method in sequence as in table-1 in sequence from top left to bottom right ac, helix, koi fish, light modulation, low frequency burst, paired dove, repeating blip, scattered light, Tomte, scratchy, whistle, wandering line

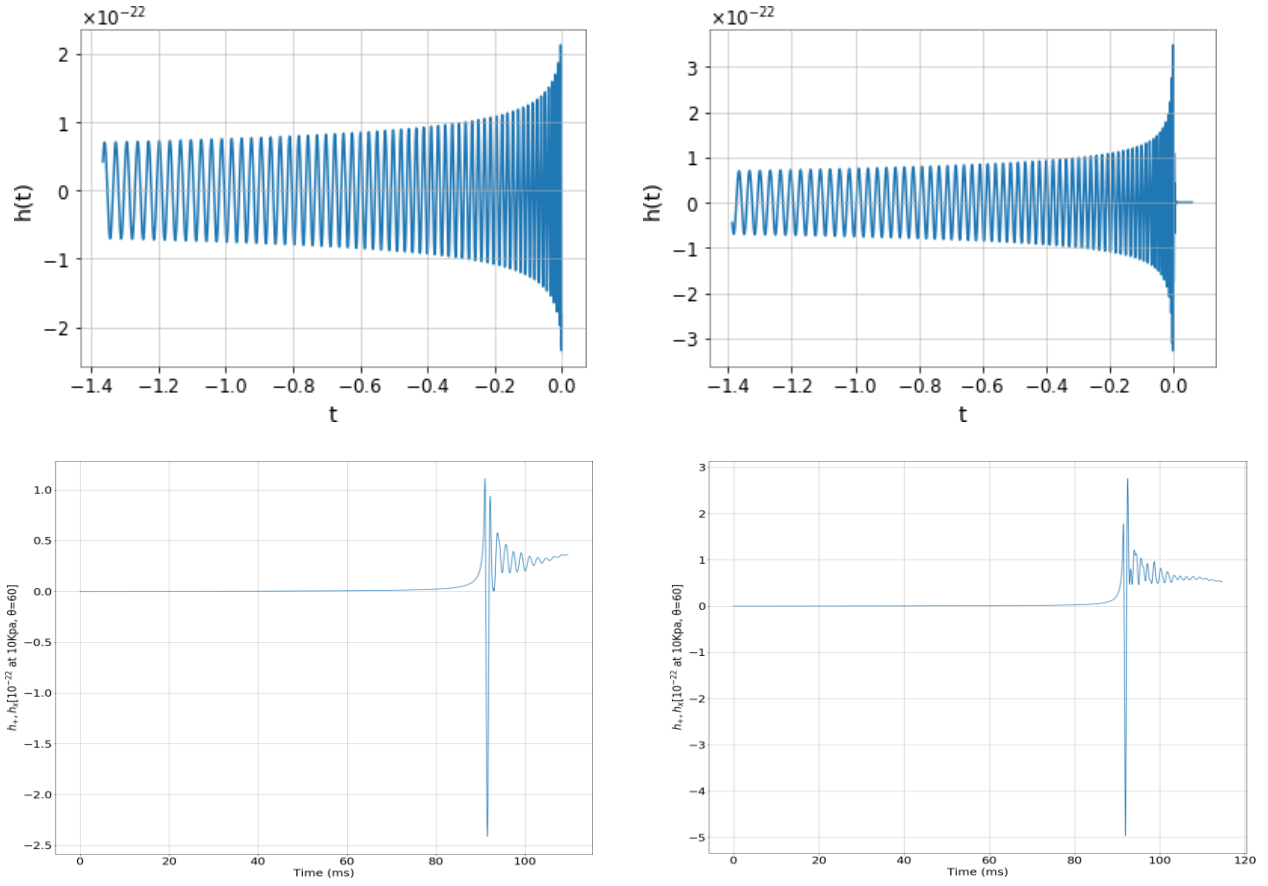


FIG 9. Waveform 1: TaylorT1  $m_1:15$   $m_2:10$  spin: (0,0,0) spin2:(0,0,0) distance:400  $f_{lower}:60$ :  $f_{upper}:50$   
 Waveform 2: EOBNRv2  $m_1:15$   $m_2:10$  spin1:(0,0,0) spin2:(0,0,0) distance:400  $f_{lower}::60$   $f_{upper}::50$   
 Waveform 3: A1B1G1<sup>R</sup> Waveform 4: A3B1G1<sup>R</sup>